Inorganic Chemistry

pubs.acs.org/IC Article

All Four Atropisomers of Iron Tetra(*o*-*N*,*N*,*N*-trimethylanilinium)porphyrin in Both the Ferric and Ferrous States

Daniel J. Martin, Brandon Q. Mercado, and James M. Mayer*

Cite This: *Inorg. Chem.* 2021, 60, 5240−5251 Read Online

ACCESS | Metrics & More | Article Recommendations | Supporting Information

ABSTRACT: Electrostatic effects are key to many biological and (electro)-chemical transformations, especially those that involve charged species. The position and orientation of the electric field with respect to the molecules undergoing charge rearrangement are often crucial to the progress of the reaction. Recently, several molecular (electro)catalysts have been designed to contain spatially positioned charged groups that can engage in specific intramolecular electrostatic interactions. For instance, iron complexes of the tetra(*o*-*N*,*N*,*N*-trimethylanilinium)porphyrin ligand, which has four cationic groups, have been used to great effect for both CO_2 and O_2 reduction. Because of the *ortho*-substitution pattern on the porphyrin ligand, there are four possible atropisomers—such as the $\alpha\beta\alpha\beta$ isomer with trimethylanilinium groups on alternating faces of the porphyrin—and thus four unique electrostatic environments. This study details the synthesis and characterization (^{1}H NMR spectroscopy, single crystal X-ray diffraction, and cyclic voltammetry) of these four metalloporphyrin isomers in both the ferric (Fe^{III}) and ferrous (Fe^{II}) forms by using a synthetic route that preserves atropisomeric purity. The atropisomers are different in some respects but show remarkable similarities in others, such as their reduction potentials. This study also shows that the widely-cited literature method used previously to prepare the molecular electrocatalyst for CO_2 and O_2 reduction yields a mixture of atropisomers rather than a single one, as was previously assumed. These results identify the ways in which intra- and intermolecular electrostatic effects affect both solution and solid-state properties as well underscoring the challenges associated with preparing metalloporphyrins with high atropisomeric purity.

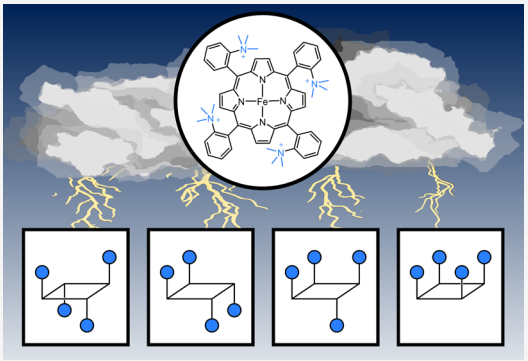

INTRODUCTION

Electrostatic and electric field effects are increasingly recognized as key to the success of many challenging, multistep reactions, especially those that involve charged intermediates or significant charge redistribution.[1−3] Such complex reactions are common in molecular electrocatalysis, which often involves single electron or proton transfer steps and the formation of charged intermediates.[4−7] Stabilizing these intermediates and decreasing kinetic barriers are required to improve reaction rates and efficiencies. Recently, these goals have prompted the design of molecular (electro)catalysts that contain spatially positioned charged groups which can stabilize charged intermediates via electrostatic interactions.[6,8−14]

One such design is the tetracationic 5,10,15,20-tetra(*o*-*N*,*N*,*N*-trimethylanilinium)porphyrin ligand (*o*-TMA), which has four positive charges positioned around the porphyrin ring. Iron complexes of this ligand are among the leading molecular electrocatalysts for both CO_2 and O_2 reduction in terms of reaction rates and efficiencies.[10,12] The success of this catalyst is due in part to the stabilization of pre-equilibria that involve anionic ligands or ligands that become sufficiently anionic upon binding[15]—effects not often emphasized in studies that used highly charged molecular designs.

Traditionally, charged groups have been added to macrocyclic ligand designs to improve solubility, especially solubility in aqueous solutions.[16,17] Pyridinium-, carboxylate-, and sulfonate-derivatized macrocycles are the most common examples of these designs, where solubility is controlled, at least in part, by the pH of the solution. Alkylated pyridinium and ammonium functional groups offer a more permanent form of charge installation and have been used in porphyrin designs to facilitate aqueous O_2/CO binding and superoxide dismutase studies.[18−22] There are a few examples of highly charged ligand designs (8+/8−) affecting basic physicochemical properties of metalloporphyrins, but these studies have only probed charge-symmetric systems in aqueous solvents.[23−27] There are no prior systems insofar as we

Received: January 24, 2021
Published: March 22, 2021

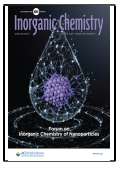

https://doi.org/10.1021/acs.inorgchem.1c00236
Inorg. Chem. 2021, 60, 5240−5251

Scheme 1. Four Different Atropisomers Available to $[Fe^{III}(o\text{-TMA})](OTf)_5$[a]

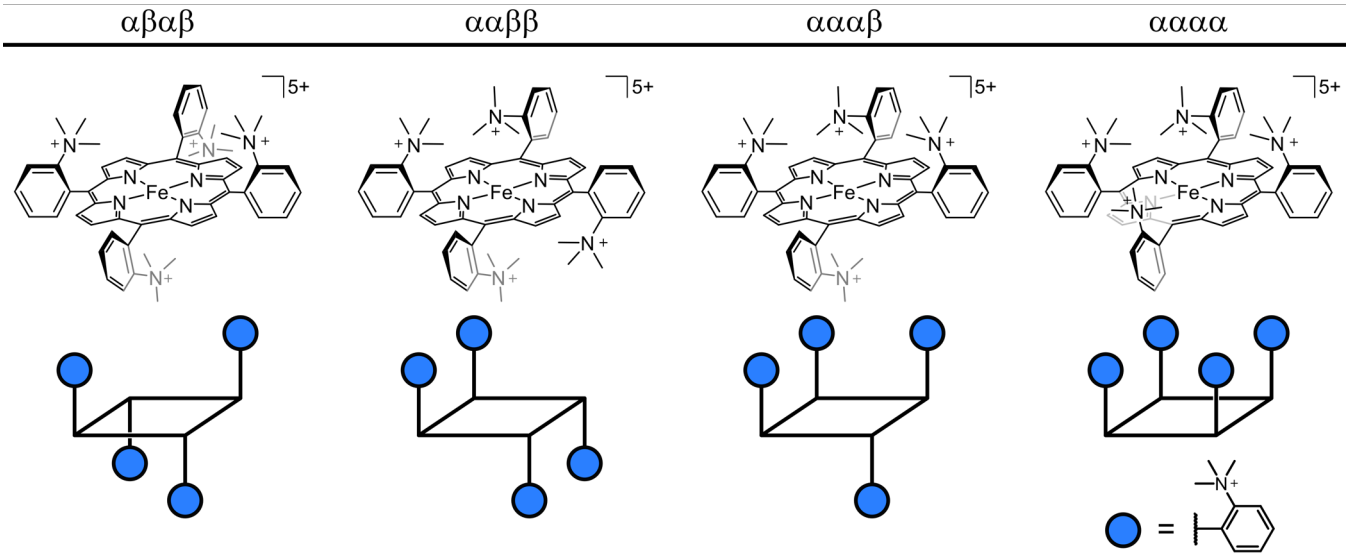

[a]The stick figures in the second row represent the different orientations of the *o*-$[N(CH_3)_3]^+$ groups.

Scheme 2. Synthesis Route Used to Prepare the $[Fe^{III}(o\text{-TMA})](OTf)_5$ Atropisomers

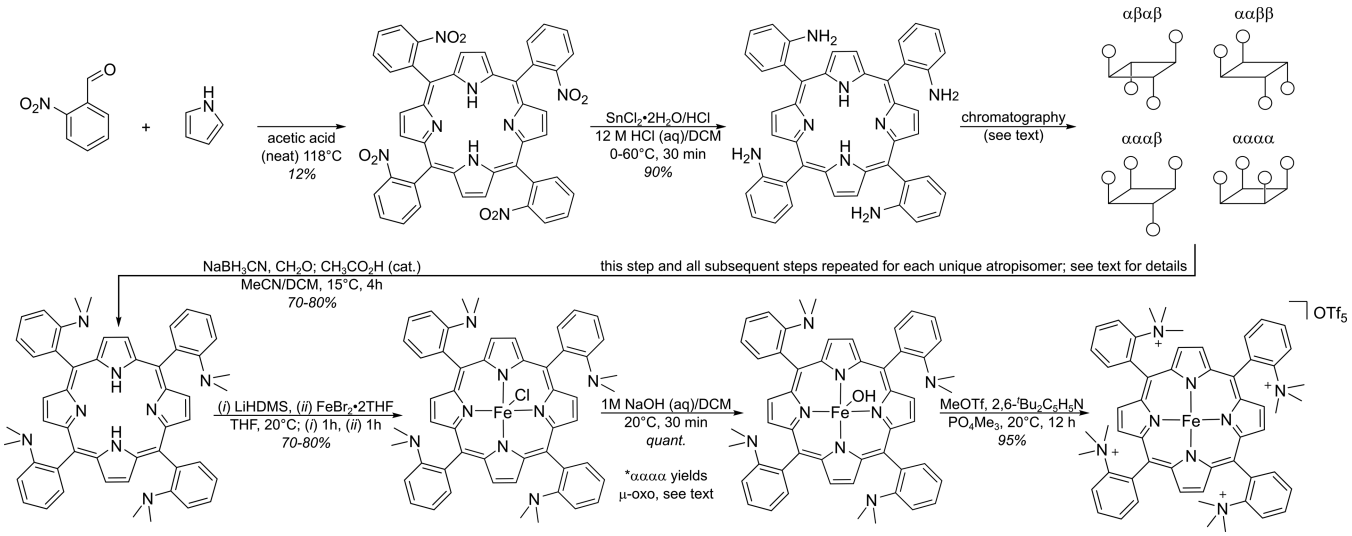

can find that analyze metal−macrocycles with different asymmetric charge distributions in nonaqueous solvents.[19]

For this reason, the (*o*-TMA) ligand and corresponding metal complexes are highly unusual. By nature of the mono-ortho substitution pattern on the aryl rings and the restricted rotational freedom at the porphyrin meso-carbons, there are four atropisomers available to the (*o*-TMA) ligand—*αβαβ*, *ααββ*, *αααβ*, and *αααα*—and thus four unique electrostatic environments (Scheme 1). Savéant and co-workers reported the first preparation of Fe(*o*-TMA) for CO_2 reduction and claimed the successful synthesis of the ferric *αβαβ* atropisomer, in which the cationic functional groups alternate on either side of the porphyrin ring.[10] The characterization data, however, were limited only to infrared spectroscopy, UV−vis absorbance, elemental analysis, and mass spectrometry techniques that cannot necessarily distinguish between the atropisomers. Crystallographic data from our group showed that the *αβαβ* isomer was indeed a component of the product synthesized via the reported method;[12] however, bulk atropisomeric purity was not established.

Here, we report improved synthetic and separation procedures for isolating all four atropisomers of Fe(*o*-TMA) in both the ferric (Fe^{III}) and ferrous (Fe^{II}) forms. Each of the atropisomers was fully characterized by using ^1H NMR spectroscopy, high-resolution mass spectrometry, and cyclic voltammetry. Seven of the eight molecules were characterized by single-crystal X-ray diffraction. The ways in which intra- and intermolecular electrostatics affect and do not affect the molecular and solid-state properties are identified and discussed. Moreover, we show that the previous synthetic route reported by Savéant et al. led to unwanted rotamerization of the aryl groups and scrambling of the isomers, resulting in a mixture of atropisomeric catalysts.

RESULTS

Synthesis. The $[Fe^{III}(o\text{-TMA})](OTf)_5$ atropisomers can be obtained in six steps by using commercially available reagents

https://doi.org/10.1021/acs.inorgchem.1c00236
Inorg. Chem. 2021, 60, 5240−5251

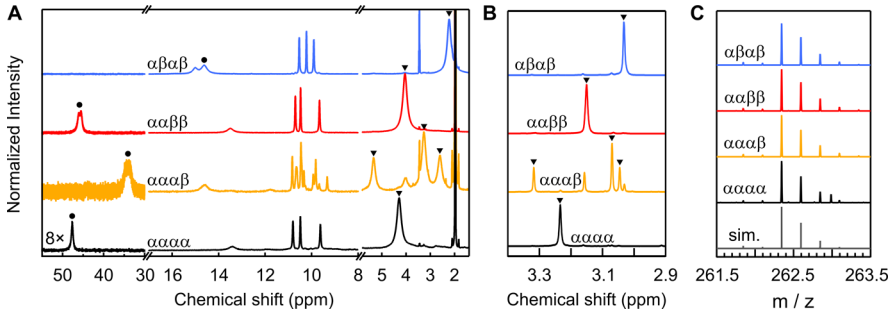

Figure 1. (A) Partial ^{1}H NMR spectra in CD_3CN of the *αβαβ*, *ααββ*, *αααβ*, and *αααα* atropisomers of [Fe^{III}(*o*-TMA)](OTf)$_5$ (see the Supporting Information for full spectra). The downfield regions are enhanced by 8× for clarity. The resonances for the *β*-pyrrolic and $N(CH_3)_3^+$ protons are identified with black circles and triangles, respectively; the sharp peak at 3.5 ppm is from Et_2O. (B) Partial ^{1}H NMR spectra of the ferrous compounds, showing the region containing the $N(CH_3)_3^+$ protons. The *αααβ* spectra show ca. 10% of the *ααββ* atropisomer, as shown by the peaks at ∼4.0 ppm in (A) and 3.18 ppm in (B). (C) High-resolution mass spectra and simulated spectrum of the [Fe(*o*-TMA)(OTf)]$^{4+}$ cation ($C_{57}H_{60}N_8FeO_3SF_3$) in the samples from (A). Full spectra are available in the Supporting Information.

and without heating later-stage intermediates (Scheme 2). The synthesis reported below is different than the more cumbersome and lower-yielding method previously used to prepare the ferric and ferrous forms of the *αβαβ* atropisomer in ref 15. Following the literature,[10] the target products first require the atropisomers of tetra(*o*-aminophenyl)porphyrin, H_2(*o*-AMP) (Figures S5−S8). These were obtained from the acid-catalyzed condensation of *o*-nitrobenzaldehyde and pyrrole, followed by reduction of the corresponding tetra(*o*-nitrophenyl)porphyrin with stannous chloride/hydrochloric acid and repeated chromatography.[28] Several chromatography conditions and eluents have been reported for isolating the various atropisomers of H_2(*o*-AMP).[10,28−31] After trying several of these conditions, we found that the most consistent method of obtaining atropisomerically pure samples (>95%) required a minimum of three separate columns with various eluent mixtures (conditions reported in the Experimental Methods section). The atropisomeric purity of the target [Fe^{III}(*o*-TMA)](OTf)$_5$ salts was dictated by this early stage chromatography, so it was imperative that the atropisomers of tetra(*o*-aminophenyl)-porphyrin were carefully separated and that they were not heated to avoid isomerization to the other atropisomers (see below).[28]

The individual H_2(*o*-AMP) atropisomers were then methylated by reductive amination using formaldehyde and sodium cyanoborohydride to yield the respective tetra(*o*-*N*,*N*-dimethylaminophenyl)porphyrins, H_2(*o*-DMA). The ^{1}H NMR spectra for these molecules were diagnostic but typically contained minor components (<5%) that could not be separated by chromatography (see Figures S10−S13).

The corresponding iron(III) chloride tetra(*o*-*N*,*N*-dimethylaminophenyl)porphyrins, Fe^{III}Cl(*o*-DMA), were prepared in 70−80% yields at 20 °C via transmetalation of the corresponding dilithium porphyrin complexes.[32] The forest green dithilium materials were (i) generated *in situ* by reacting the H_2(*o*-DMA) isomers with 2 equiv of lithium hexamethyldisilazide in THF and then (ii) reacted with ferrous bromide ($FeBr_2$·2THF). Iron insertion proceeds more readily with the lithiated porphyrins than with the free base analogues, likely a result of forming LiCl or LiBr, which are poorly soluble in THF. The ^{1}H NMR spectra of the product metalloporphyrins were broad due to the paramagnetism of the iron center. Chloride binding introduced additional asymmetry, which was identified in the diagnostic pyrrole region of the spectra (75−85 ppm; see the Supporting Information).

The Fe^{III}Cl(*o*-DMA) compounds were then converted to the respective hydroxo complexes, Fe^{III}OH(*o*-DMA), by dissolving them in DCM and stirring with 1 M NaOH(aq) for 30 min.[33] This ligand substitution more consistently yielded the desired pentatriflate salts in the final methylation step. The hydroxo form of the *αααα* atropisomer rapidly hydrolyzed to form the corresponding *μ*-oxo dimer (by ^{1}H NMR spectroscopy and MS), which was the isolated product after chromatography. The other isomers did not form *μ*-oxo dimers, presumably due to steric bulk on both sides of the porphyrin ring.

Finally, the Fe^{III}OH(*o*-DMA) complexes (and *μ*-oxo dimer of the *αααα* isomer) were quaternized to the target [Fe^{III}(*o*-TMA)](OTf)$_5$ molecules by using excess methyl triflate in trimethyl phosphate containing a few drops of 2,6-di-*tert*-butylpyridine.[15] The sterically bulky base was key to the success of the reaction, as it sequestered disadvantageous triflic acid present in the commercial methyl triflate.[18] After stirring (12 h at 20 °C), excess methyl triflate was quenched with methanol, and the products were precipitated by adding the reaction mixture dropwise into stirring Et_2O. Quenching the methyl triflate with methanol generated triflic acid, which protonated the hydroxo ligands and hydrolyzed the *μ*-oxo dimer of the *αααα* isomer (see the Supporting Information). The product of this reaction was quantitative and yielded the corresponding pentatriflate salts (Figures S20−S23). The crude solids were slowly recrystallized from MeCN/Et_2O mixtures in a glovebox, and the crystalline samples of the [Fe^{III}(*o*-TMA)](OTf)$_5$ isomers were characterized by ^{1}H NMR spectroscopy, single-crystal X-ray crystallography, and cyclic voltammetry (see below and the Supporting Information).

The corresponding iron(II) atropisomers were prepared by stirring the iron(III) salts over Zn(Hg) amalgam in the glovebox.[15,34−36] Within an hour, the reactions were complete, and the solutions had lightened in color from maroon to cherry red. After filtering and rinsing the amalgams, we recrystallized the iron(II) porphyrin-containing solutions by vapor diffusion, and the products were isolated as blocky purple crystals. These crystalline solids were also characterized by ^{1}H NMR spectroscopy (Figures S29−S32) and single-crystal X-ray crystallography (see below and the Supporting Information).

^{1}H NMR Spectra of the Fe(III) and Fe(II) Porphyrin Salts. The ferric (Fe^{III}) pentatriflate atropisomers each had a unique, paramagnetic ^{1}H NMR spectrum, with signals corresponding to the *β*-pyrrolic, aromatic, and trimethylanilinium protons (Figure 1A and Figures S20−S23). The *β*-

https://doi.org/10.1021/acs.inorgchem.1c00236
Inorg. Chem. 2021, 60, 5240−5251

pyrrolic protons were assigned by integration (8*H*) and were typically the most downfield signals (ranging from 13 to 50 ppm). These signals appeared as broad singlets for the *αβαβ* and *αααα* atropisomers and as a set of two overlapping singlets for the *ααββ* isomer, in which there are two different sets of pyrroles. The *β*-pyrrolic signal for the *αααβ* atropisomer was broad and unsymmetric. The aromatic protons were less downfield (ranging from 7 to 16 ppm) and were generally sharper. The spectra of the *αβαβ*, *ααββ*, and *αααα* atropisomers each contained four unique aromatic peaks (4*H* per peak; one signal was broad and downfield), while the spectrum of the *αααβ* atropisomer contained a more complicated set of peaks (16*H* total). The 36 protons that corresponded to the trimethylanilinium groups were the most upfield signals in the spectra (1−5 ppm). These protons appeared as broad singlets for each of the *αβαβ*, *ααββ*, and *αααα* atropisomers and as three broad singlets (1:1:2 ratio) in the *αααβ* spectrum.

The ferrous (Fe^{II}) atropisomers had ^{1}H NMR spectra in CD_3CN that were diamagnetic with no evidence of remaining paramagnetic impurities, showing complete reduction (Figures S29−S32). Like the ferric complexes, the ^{1}H NMR spectra contained signals that corresponded to the *β*-pyrrolic (8*H*), aromatic (16*H*), and trimethylanilinium (36*H*) protons, which were assigned by relative integrations (Figure 1B).

The ^{1}H NMR spectra of the product porphyrins show their atropisomeric purity. For the *αβαβ*, *ααββ*, and *αααα* porphyrins, the synthesis method described in this report allowed for preparation with >95% isomeric purity. While the actual purities are likely higher for these atropisomers, we report these values as lower limits due to limitations of ^{1}H NMR integration. The *αααβ* complex was isolated with >90% purity, with the *ααββ* atropisomer accounting for nearly all the remaining signal in the ^{1}H NMR spectrum. As expected, the mass spectra are indistinguishable and cannot be used to identify any individual isomer (Figure 1C).

Thermal Atropisomer Rotamerization. The rates of tetraarylporphyrin rotamerization have been documented for several ortho-substituted porphyrins, including the H_2(*o*-AMP) isomers used in this work.[30,31,37−39] Generally, rotamerization rates increase with temperature and decrease when sterically bulky groups are added at the *ortho*-position of the aryl rings.[37,39]

Here, the relative rates of isomerization for the *αβαβ* atropisomers of H_2(*o*-AMP), H_2(*o*-DMA), and [Fe^{III}(*o*-TMA)](OTf)$_5$ were measured using a ^{1}H NMR time course (Figures S34−S36). A solution of each molecule was prepared in deuterated solvent, loaded into a J. Young tube, and heated to 80 °C using a preheated oil bath for 48 h with regular spectra being collected. A portion of the aromatic region of the spectra was fit by using MestReNova to yield the percent *αβαβ* isomer remaining at each time point (see the Supporting Information), which are plotted in Figure 2.

As shown in Figure 2, both the *αβαβ* H_2(*o*-AMP) and H_2(*o*-DMA) porphyrins rotamerize with similar time profiles and approach the theoretical limit (12.5%) expected for the statistical mixture of isomers.[28] At 80 °C, the half-life of both reactions is <0.5 h, and complete isomerization was reached within 6 h. While rapid isomerization of H_2(*o*-AMP) was expected at 80 °C, it was surprising that the more sterically encumbered H_2(*o*-DMA) isomerized just as quickly. In contrast, there was no evidence of isomerization for the *αβαβ* atropisomer of [Fe^{III}(*o*-TMA)](OTf)$_5$ under these conditions, even with additional heating to 100 °C for 48 h (Figure S36). The more sterically encumbered *αααα* [Fe^{III}(*o*-TMA)](OTf)$_5$

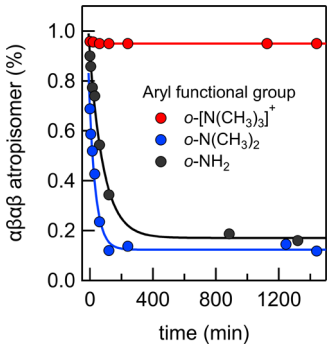

Figure 2. Isomerization profiles for the rotamerization of [Fe^{III}(*o*-TMA)](OTf)$_5$, H_2(*o*-DMA), and H_2(*o*-AMP) at 80 °C. The solvent was CD_3CN for [Fe^{III}(*o*-TMA)](OTf)$_5$ and $CDCl_3$ for H_2(*o*-AMP) and H_2(*o*-DMA) porphyrins. ^{1}H NMR spectra are available in the Supporting Information.

atropisomer was also stable at these higher temperatures (Figure S37).

The rapid isomerization rate for the *o*-$N(CH_3)_2$-substituted porphyrin was surprising and led us to question the atropisomeric fidelity of the original synthesis reported by Savéant et al. The original synthesis required extended heating of *αβαβ* Fe^{III}Cl(*o*-DMA) during the final methylation step (24 h at 100 °C in DMF).[10] These conditions far exceed the temperatures and times that were shown to cause rotamerization in this work. To probe whether atropisomeric purity could be preserved under these harsh conditions, the reported synthetic procedures were repeated by using an isolated sample of the *αβαβ* Fe^{III}Cl(*o*-DMA) precursor. After work-up, the ^{1}H NMR spectrum of the product was compared to the genuine spectra of the atropisomers isolated in this work. Rather than the singular *αβαβ* atropisomer, as was reported, the product was a mixture of isomers (Figure 3). The *αβαβ* and *αααβ* isomers made up

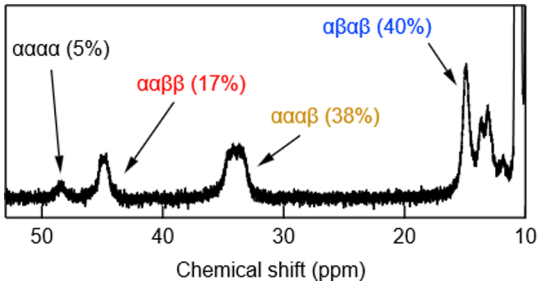

Figure 3. Partial ^{1}H NMR spectrum of the [Fe^{III}(*o*-TMA)](OTf)$_5$ product obtained by using the synthesis conditions reported by Savéant et al.[10] The isomers are identified by the respective pyrrolic peaks (8*H*) which were integrated by using MestReNova. Spectrum was recorded in CD_3CN at 400 MHz. Full spectra are available in the Supporting Information.

approximately equal fractions (40% and 38%, respectively), followed by the *ααββ* (17%), and *αααα* (5%) atropisomers (Figures S27 and S28). These data show that original synthesis does not yield a single isomer, as was assumed, but rather a mixture of all four atropisomers. The ramifications of this are discussed below.

Single-Crystal X-ray Characterization. Crystals suitable for single-crystal X-ray diffraction were obtained for both the ferric and ferrous forms of the *αβαβ*, *ααββ*, and *αααα* atropisomers and for the ferrous-only form of the *αααβ* isomer

https://doi.org/10.1021/acs.inorgchem.1c00236
Inorg. Chem. 2021, 60, 5240−5251

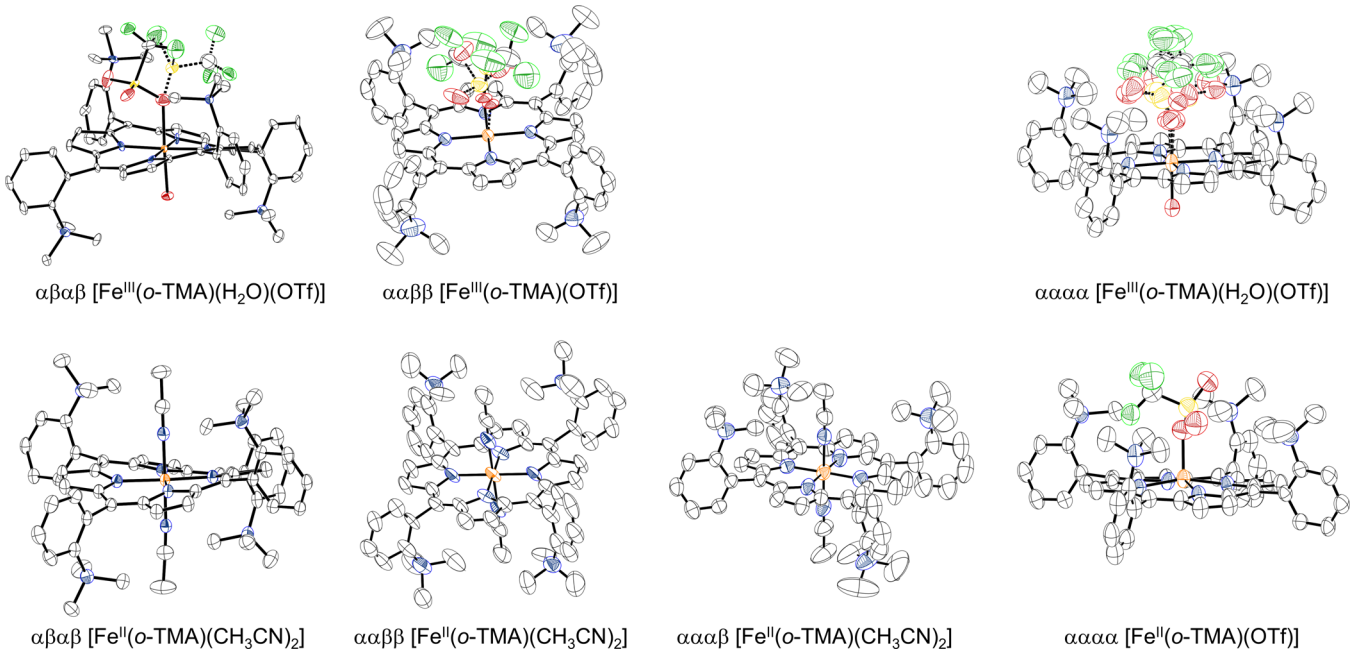

Figure 4. Single-crystal X-ray structures of the *αβαβ*, *ααββ*, and *αααα* atropisomers in both the ferric and ferrous forms and the *αααβ* isomer in the ferrous form only. In the ferric structures on the top, the multiple disordered orientations of the single bound triflate ligand are shown. Fe, orange; N, blue; C, white; H atoms and triflates that were not bound were omitted for clarity; thermal ellipsoids shown at 50% probability. The *αβαβ* [Fe^{II}(*o*-TMA)$(CH_3CN)_2$] structure is reported in ref 15.

by vapor diffusion of Et_2O into MeCN (Figure 4). The ferrous *αβαβ* structure has already been reported[15] and is repeated here for reference. A bis-aquo complex of the ferric *αβαβ* porphyrin was reported in ref 12, but the triflate-bound structure reported here is new. Five triflate anions were identified in each of the ferric porphyrin crystal structures, and four were identified in each of the ferrous structures. Many of the triflate anions were disordered and had to be modeled, as described in the Supporting Information. The crystals obtained for the ferric *αααβ* atropisomer were too disordered for single-crystal studies.

All seven structures have ligands bound to the iron center. For the three ferric structures, a single triflate was bound to the metal. The *α* and *β* faces of the *αβαβ* and *ααββ* structures are symmetry equivalent; thus, there is no site selectivity for the bound triflate. The *αααα* atropisomer, however, has inequivalent sides with different steric and electrostatic environments. In the solid-state structure, a triflate ligand was bound to the more crowded, more cationic *α* face, and a water molecule was bound to the *β* face (Figure 4). The triflate being bound to the *α* face is the opposite of what one might expect based on sterics. The *α* face of the *αααα* atropisomer is by far the most congested site across the series of structures in this work and is intuitively the least likely site for a large anion to bind. The structures of the ferrous *αβαβ*, *ααββ*, and *αααβ* complexes each had two acetonitrile ligands bound to the iron. The *αααα* isomer did not have any acetonitrile ligands; rather, a triflate ligand was bound to the metal, again on the *α*-face.

The packing of anions and cations in the *αβαβ*, *ααββ*, and *αααβ* structures showed repeating units of metalloporphyrin with triflate molecules distributed near the trimethylanilinium groups. In contrast, both the ferric and ferrous forms of the *αααα* atropisomer packed as a bilayer structure with a densely packed layer of triflates appearing between the *α*-faces (Figure 5). In the ferric structure, the *β* faces are parallel and separated by 5.17 Å, longer than typical porphyrin *π*−*π* interaction distances.[40] The ferrous structure has nonparallel *β* faces and no evidence of *π*−*π* interactions.

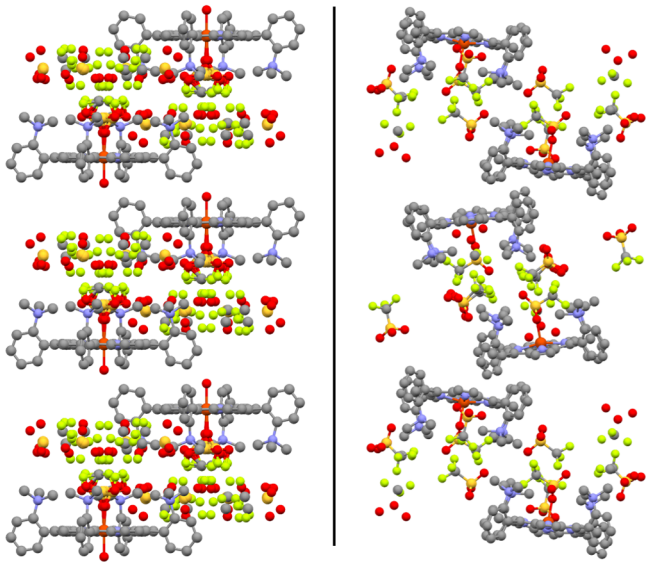

Figure 5. (left) Packing structure of the ferric *αααα* [Fe^{III}(*o*-TMA)(H_2O)(OTf)][$(OTf)_4$ complex. (right) Packing structure of the ferrous *αααα* [Fe^{II}(*o*-TMA)(OTf)][$(OTf)_3$ complex. The layered structure has the *α*-faces (with the anilinium groups) oriented toward one another in a repeating *βα*|*αβ* pattern, with the triflates concentrated between the *α* faces. All the atoms of the different orientations of the disordered triflates are shown. Color coding: C, gray; N, blue; O, red; S, orange; F, light green; Fe, dark orange; H atoms omitted for clarity.

Electrochemistry. Cyclic voltammograms (CVs) of the four atropisomers were measured in acetonitrile (MeCN) containing 0.1 M tetrabutylammonium hexafluorophosphate [*n*-Bu_4N][PF_6]. The voltammograms were internally referenced to decamethylferrocene ($Me_{10}Fc$), which was independently

https://doi.org/10.1021/acs.inorgchem.1c00236
Inorg. Chem. 2021, 60, 5240−5251

Table 1. Reduction Potentials for the Four Atropisomers of Fe(*o*-TMA) for Fe(*p*-TMA) and for Fe(TPP)[a]

structural isomer	atropisomer	solvent	$E_{1/2}(Fe^{III}/Fe^{II})$	$E_{1/2}(Fe^{II}/Fe^{I})$	$E_{1/2}(Fe^{I}/Fe^{0})$
Fe(*o*-TMA)	*αβαβ*	MeCN	0.142	−1.194	−1.594
	ααββ	MeCN	0.143	−1.201	−1.640
	αααβ	MeCN	0.130	−1.200	−1.632
	αααα	MeCN	0.135	−1.187	−1.635
	average	MeCN	0.14 ± 0.01	−1.20 ± 0.01	−1.63 ± 0.02
	αβαβ	DMF	−0.351	−1.166	−1.683
	ααββ	DMF	−0.337	−1.198	−1.705
	αααβ	DMF	−0.341	−1.194	−1.698
	αααα	DMF	−0.329	−1.195	−1.695
	average	DMF	−0.34 ± 0.01	−1.19 ± 0.01	−1.70 ± 0.01
[Fe(*p*-TMA)]		MeCN	−0.089	−1.316	ca. −1.8[a]
		DMF	−0.55[b]	−1.40[b]	−1.92[b]
Fe(TPP)		PrCN[d]	−0.259		
		DMF	−0.61[e]	−1.45[e]	−2.07[e]

[a]In MeCN or DMF containing 0.1 M $[n\text{-}Bu_4N][PF_6]$. Potentials (±0.005 V) referenced vs Fc^+/Fc. [b]This redox feature was broad and poorly reversible. Reported value equal to the midpoint potential from the maximum and minimum current responses. [c]Reported values in DMF for $[Fe(p\text{-TMA})](Cl)_5$.[46] [d]Reported in *n*-butyronitrile containing 0.1 M $[n\text{-}Bu_4N][PF_6]$ for [Fe(TPP)]OTf.[15] [e]Reported for Fe(TPP)Cl in ref 46.

referenced to ferrocene (Fc) by using a separate solution (to avoid overlaps between $E_{1/2}(Fc^{+/0})$ and metalloporphyrin redox features). Each of the atropisomers showed three reversible reductions, which were assigned to the corresponding Fe^{III}/Fe^{II}, "Fe^{II}/Fe^{I}", and "Fe^{I}/Fe^{0}" redox couples, as is typical for iron porphyrins in nonaqueous solvent (Table 1 and Figure 6).[35,41]

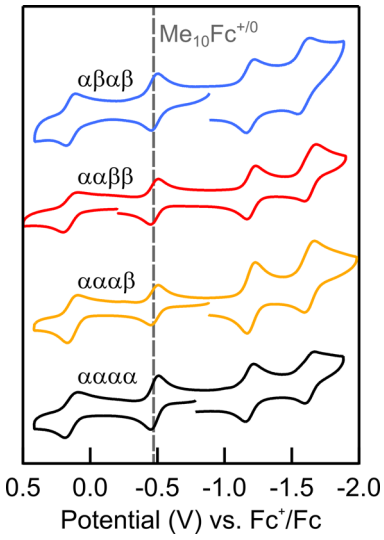

Figure 6. Cyclic voltammograms for the four atropisomers of $[Fe^{III}(o\text{-TMA})](OTf)_5$ in MeCN containing 0.1 M $[n\text{-}Bu_4N][PF_6]$. All voltammograms were collected at 0.1 V s^{-1} and referenced to Fc^+/Fc.

The iron(I) and iron(0) labels are in quotation marks to indicate that these complexes may involve a significant amount of ligand-centered reduction.[42,43] Characterization of the low-valent species was not pursued in this work.

As a result of the four cationic, electron-withdrawing *o*-$[N(CH_3)_3]^+$ groups, each of the respective redox couples has $E_{1/2}$ values that are several hundred millivolts more positive than those typical for iron porphyrin complexes in polar organic solvents (acetonitrile, *n*-butyronitrile, and *N*,*N*-dimethylformamide, among others).[41,44,45] Despite similar inductive effects, the various $E_{1/2}$ values are also more than 0.1−0.2 V more positive than the corresponding values for Fe(*p*-TMA), a control molecule bearing *para*-$[N(CH_3)_3]^+$ groups (Table 1). Yet, while the magnitudes of the positive shifts are unusual, the Fe(*o*-TMA) $E_{1/2}$ values were quite similar between the four atropisomers. The range of $E_{1/2}(Fe^{III}/Fe^{II})$ and $E_{1/2}(Fe^{II}/Fe^{I})$ values was only ∼10 mV across the series. The range was ∼40 mV for the $E_{1/2}(Fe^{I}/Fe^{0})$ values; however, this larger deviation was due only to the positively shifted $E_{1/2}(Fe^{I}/Fe^{0})$ of the *αβαβ* atropisomer. In *N*,*N*-dimethylformamide (DMF) containing 0.1 M electrolyte, the same conditions reported by Savéant et al. in ref 10, the $E_{1/2}(Fe^{I}/Fe^{0})$ values span only 22 mV. Under these conditions, three of the four isomers have $E_{1/2}(Fe^{I}/Fe^{0})$ values that are within the uncertainty of the measurement (Table 1).

DISCUSSION

Effects of Oriented Charges on the Properties of Fe(*o*-TMA). The spectroscopic, electrochemical, and structural data for the four Fe(*o*-TMA) atropisomers provide unusual insights into the role of the *orientation* of electrostatic groups on molecular properties. In contrast to most studies of electrostatics in small molecule and inorganic chemistries, this work yields information about the effects of the relative position of charges without changing their type or number or distance from the metal center.

By nature of the *o*-TMA ligand design, there are four potential atropisomers available to the single iron porphyrin complex, each of which has a unique symmetry and electrostatic environment. The *αβαβ* (D_{2d}) isomer has the highest point group symmetry of the series, followed by the *ααββ* (C_{2h}), *αααα* (C_{4v}), and *αααβ* (C_s) atropisomers. The following discussion is divided into two sections that highlight how these unique electrostatic environments affect or do not affect the electrochemical and solid-state structural properties.

Effects of Oriented Charges on Electrochemical Data. The electrochemistry of the four atropisomers was almost completely unaffected by the orientation of the *o*-$[N(CH_3)_3]^+$ groups. The isomers have very similar potentials, both in MeCN and in DMF. This is a surprising result. For instance, the *αααα* isomer should have a substantial dipole moment along the 4-fold axis while the *αβαβ* isomer has no net dipole moment (ignoring any counterion or ligand binding). These results do *not* imply the

https://doi.org/10.1021/acs.inorgchem.1c00236
Inorg. Chem. 2021, 60, 5240−5251

charged groups are unimportant, only that *their relative orientations with respect to the metal center do not significantly affect the electrochemistry*.

The *lack* of variation between the atropisomer $E_{1/2}$ values indicates that the energy required to bring a negative point charge (e.g., the e^-) from infinity to a polycationic, quasi-spherical species is largely unaffected by the precise orientation of the charges within the cation. Rather, the overall energetics chiefly concern the addition of a monoanion to a compact polycation. These data also indicate that the electrochemical double layers surrounding the respective atropisomers (e.g., $[OTf]^-$ or $[PF_6]^-$ anions from the electrolyte) are not sufficiently different that they affect the reduction thermochemistry.

The most important function of the four *o*-$[N(CH_3)_3]^+$ groups on the electrochemistry is to make the molecules easier to reduce (more positive $E_{1/2}$ values). For applications in electrocatalysis, more positive $E_{1/2}$ values imply smaller overpotentials.[12] This increase in $E_{1/2}$ over related compounds like the neutral Fe(TPP) complex is observed for all three redox couples: Fe^{III}/Fe^{II}, "Fe^{II}/Fe^{I}", and "Fe^{I}/Fe^{0}" (Table 1).

The more positive $E_{1/2}$ values could result from either electrostatic, through-space effects or inductive, through-bond effects, or some combination of the two. In a previous study, we estimated the inductive effects from the four $[N(CH_3)_3]^+$ groups account for roughly half of the difference between the $E_{1/2}(Fe^{III}/Fe^{II})$ values of the $\alpha\beta\alpha\beta$ isomer and Fe(TPP) in *n*-butyronitrile.[15] To understand the electrostatic component, we compare the $E_{1/2}$ values of the Fe(*o*-TMA) isomers with the structural *para*-substituted isomer, Fe(*p*-TMA) (Scheme 3).

Scheme 3. Electrostatic, Charged Sphere Model for the Reduction of Fe(*o*-TMA) and Fe(*p*-TMA) Structural Isomers

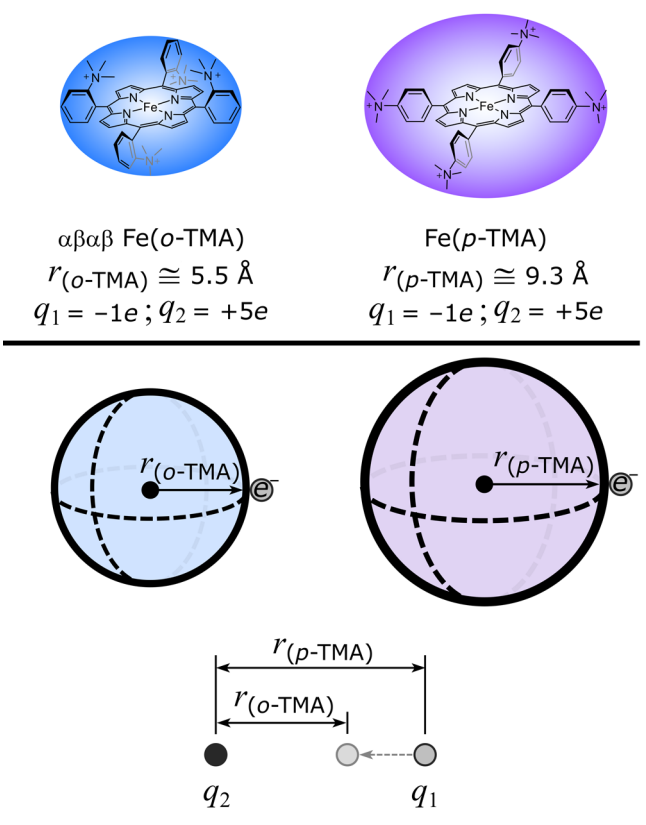

The inductive effects of the $[N(CH_3)]^+$ groups should be similar in Fe(*o*-TMA) and Fe(*p*-TMA), yet the *ortho* isomers have substantially more positive reduction potentials, by +0.23 V ($\Delta E_{1/2}[Fe^{III}/Fe^{II}]$), +0.12 V ($\Delta E_{1/2}[Fe^{II}/Fe^{I}]$), and +0.17 V ($\Delta E_{1/2}[Fe^{I}/Fe^{0}]$) in MeCN. Similar trends and values were also observed in DMF (Table 1): +0.21 V ($\Delta E_{1/2}[Fe^{III}/Fe^{II}]$), +0.21 V ($\Delta E_{1/2}[Fe^{II}/Fe^{I}]$), and +0.22 V ($\Delta E_{1/2}[Fe^{I}/Fe^{0}]$).[15,41]

An electrostatic, charged sphere model offers a partial explanation of the higher potential for Fe(*o*-TMA) vs Fe(*p*-TMA). For such a model, we consider each of these complexes as positively charged spheres and the electron being added to the surface of the sphere. While this is a very crude model, it is a good first approximation because a spherically symmetric charge density behaves as a point charge concentrated at the center. The change in potential energy (ΔU) to move a charge (q_1) from infinite distance to the surface of a sphere of charge q_2 is given by eq 1, where ϵ_0 is the permittivity of the vacuum and ϵ is the static dielectric constant of the medium. The distance r is the radius of the sphere, the distance from the center to the surface. For the chemistry being analyzed here, $q_1 = -1e$ for the electron being added, and q_2 for the ferric complexes is $+5e$, for both Fe(*o*-TMA) and Fe(*p*-TMA). The only difference between these compounds in this model is the size of the sphere that encloses most of the charge, which is clearly smaller for Fe(*o*-TMA) and Fe(*p*-TMA) (Scheme 3). By approximating the diameter of each sphere as the distance between the N atoms of the $[N(CH_3)_3]^+$ groups on the phenyl rings in the 5- and 15-meso positions, we estimate that the radius for the Fe(*o*-TMA) and Fe(*p*-TMA) complexes is $r_{ortho} \cong 5.5$ Å and $r_{para} \cong 9.3$ Å (see Supporting Information Section VI for all distances). Thus, the more compact charges of the *ortho* isomer should yield a larger electrostatic effect than the four charges in the larger *para* isomer, as observed experimentally.

$$\Delta U = \frac{q_1 q_2}{4\pi\epsilon\epsilon_0}\frac{1}{r} \tag{1}$$

This electrostatic picture provides a qualitative estimate of the expected effect. Using $q_2 = +5$, $r_{ortho} \cong 5.5$ Å, $r_{para} \cong 9.3$ Å, and $\epsilon_{MeCN} = 38$[47] (though it might be larger with 0.1 M $[^nBu_4N][PF_6]$[48]), we estimate that the Fe^{III}/Fe^{II} reduction potential is larger by ~0.13 V for the *ortho*-isomer because of its higher charge density. For such a simple model, this is remarkably close to the 0.2−0.1 V observed experimentally.

This simple model is not as successful at predicting other trends in the electrochemical data. One might have expected that the $\alpha\alpha\alpha\alpha$ isomer would have a more compact sphere of charge than the $\alpha\beta\alpha\beta$ isomer and therefore a larger electrostatic contribution. However, the potentials for these isomers are quite close, and the $\alpha\alpha\alpha\alpha$ isomer has *less* positive than the larger $\alpha\beta\alpha\beta$ isomer. Of course, a key piece missing from this model is the direct binding of anions such as triflate to the iron center, as observed crystallographically. It seems likely that such anion binding occurs to a different extent for the different atropisomers. As another example, eq 1 and intuition predict that the electrostatic effects should be greater for reduction of the Fe^{III} complex, a 5+ cation, than for the 3+ Fe^{I} species (q_2 = 5+ vs 3+ in eq 1). Yet such a trend is hard to discern in the data in Table 1, either in MeCN or in DMF. Perhaps this effect is too small to be observed comparing different redox couples, where some of the assumptions in the simple spherical charge model may not hold very well.

We advocate using this simple model not to make quantitative predictions, but as a starting point to build intuition and to

https://doi.org/10.1021/acs.inorgchem.1c00236
Inorg. Chem. 2021, 60, 5240−5251

identify when other effects such as anion binding play important roles. It is remarkable, with all the different effects involved, that the reduction potentials are almost invariant to the atropisomer identity in both MeCN and DMF (Table 1). This is the case for the Fe^{III}/Fe^{II}, "Fe^{II}/Fe^{I}", and "Fe^{I}/Fe^{0}" transformations even though the lower-valent complexes may involve significant charge transfer to the redox noninnocent porphyrin ring. The similar potentials suggest that the simple electrostatic hard-sphere model may capture a significant part of the physics involved. Future work will explore the role(s) of ion pairing and the "double layer" around these polycationic complexes.

Effects of Oriented Charges on Crystallographic Data. In contrast to the electrochemical data, the crystallographic structures were distinct for each isomer and indicate that electrostatic interactions control both the primary coordination environment and packing structure of the solids. The ferric and ferrous structures of the $\alpha\alpha\alpha\alpha$ atropisomer are the most indicative of these effects. In both the ferric and ferrous complexes, the $\alpha\alpha\alpha\alpha$ isomer shows a bound triflate ligand to the more crowded α face and a layered packing structure. These data contrast the structures obtained for the three remaining isomers, which have triflate ligands bound only to the ferric structures and do not pack in layers.

The difference in primary coordination environments for the different atropisomers, and between the respective ferric and ferrous structures, is evidence to the strength of local, *intramolecular* electrostatic interactions between the bound triflate ligand and the *o*-$[N(CH_3)_3]^+$ groups. For the $\alpha\beta\alpha\beta$, $\alpha\alpha\beta\beta$, and $\alpha\alpha\alpha\beta$ atropisomers, only the ferric structures have a bound triflate ligand. The ferrous structures, which have a smaller overall charge and a softer metal ion,[49] have two bound acetonitrile ligands. In contrast, both the ferric and ferrous forms of the $\alpha\alpha\alpha\alpha$ atropisomer have a triflate ligand that is bound to the sterically crowded α-face. These data indicate not only that local, short-range interactions exist between the triflate ligand and the nearby *o*-$(N(CH_3)_3)^+$ cations on the α-face of the $\alpha\alpha\alpha\alpha$ atropisomer but also that this electrostatic attraction overcomes the intrinsic preference of the ferrous ion for soft acetonitrile ligands. Yet the $\alpha\alpha\alpha\beta$ isomer, with three *o*-$[N(CH_3)_3]^+$ groups on the same side and lower steric hindrance, does not sufficiently stabilize triflate as to overcome the intrinsic ligand preferences.

Local electrostatic interactions also impact the packing structure of the solids. In both the ferric and ferrous forms of the $\alpha\beta\alpha\beta$, $\alpha\alpha\beta\beta$, and $\alpha\alpha\alpha\beta$ atropisomers, the polycationic iron porphyrin complex—$[Fe^{III}(o\text{-TMA})(OTf)]^{4+}$ or $[Fe^{II}(o\text{-TMA})(CH_3CN)_2]^{4+}$—is surrounded by four triflate anions that are evenly distributed around each 4+ cation. The 3D lattice of alternating ions is reminiscent of crystal packing for common ionic solids. In contrast, the ferric and ferrous $\alpha\alpha\alpha\alpha$ solids pack in dense, 2D layers of cations and anions. This unique packing emphasizes the strength of the local electrostatic interactions that exist between the alternating layers of Fe(*o*-TMA) α-faces and triflate anions, which persists despite the change in overall charge of the cation: $[Fe^{III}(o\text{-TMA})(OTf)]^{4+}$ vs $[Fe^{II}(o\text{-TMA})(OTf)]^{3+}$.

Catalyst Identity in Prior Electrocatalytic CO_2 and O_2 Reduction Studies. The $\alpha\beta\alpha\beta$ atropisomer of Fe(*o*-TMA) was first designed and reported as a CO_2 reduction electrocatalyst.[10] To date, it remains one of the leading molecular CO_2RR catalysts in both rates and overpotentials and has gained significant attention in the literature (>200 references as of 12/2020). Yet, as shown above, duplicating the reported conditions used to prepare this catalyst results in a mixture of Fe(*o*-TMA) atropisomers and not just the claimed $\alpha\beta\alpha\beta$ product.

The unwanted rotamerization is caused by the extended heating during the final methylation step: the published procedure involves heating the $\alpha\beta\alpha\beta$ FeCl(*o*-DMA) precursor at 100 °C for 24 h. The studies reported here show that these conditions result in a mixture that contains only 40% of the desired $\alpha\beta\alpha\beta$ isomer. Still, this 40% is substantially more than the 12.5% expected from a statistical mixture, and we have shown that $\alpha\beta\alpha\beta$ $[Fe^{III}(o\text{-TMA})](OTf)_5$ does not isomerize at 100 °C. Therefore, rotamerization of the $\alpha\beta\alpha\beta$ FeCl(*o*-DMA) precursor must occur with rates that are commensurate with the methylation reaction under the reported conditions. Rotamerization can only be avoided by using milder conditions, such as those described in this work.

The data reported here rationalize why this misidentified catalyst product was not detected in ref 10. In that study, the final metalloporphyrin catalyst was characterized by IR, UV−vis, mass spectrometry, and elemental analysis, none of which distinguishes between the atropisomers $[Fe^{III}(o\text{-TMA})](OTf)_5$. Electrochemically, the $E_{1/2}$ values for the atropisomers are sufficiently similar in both MeCN and DMF that broadening of cyclic voltammograms of the mixture might not have been evident. The largest difference in potentials is 46 mV between the $\alpha\beta\alpha\beta$ and $\alpha\alpha\beta\beta$ isomers in MeCN for the "Fe^{I}/Fe^{0}" couple. Our group was also guilty of this oversight in ref 12, following the original synthesis and characterization of the material. We have moved to using milder synthetic conditions to avoid isomerization, as for the compounds used in ref 15.

The correct catalyst identification is directly relevant to the electrocatalysis reported by both the original studies and our subsequent paper. Both refs 10 and 12 report (electro)catalysis using a mixture of atropisomers rather than with a single catalyst species. Our study,[12] as noted above, used a catalyst mixture with a very narrow range of $E_{1/2}(Fe^{III}/Fe^{II})$ values and considered only how $E_{1/2}$ changed with buffer pK_a. These values were obtained by using *in situ* experiments that (in retrospect) showed that atropisomeric purity of the catalyst was not required. Reference 10 hypothesized that the enhanced catalysis is "most likely [due to] the stabilization of the initial Fe(0)−CO_2 adduct by the interaction of the negative charge borne by the oxygens of CO_2 in this adduct with the nearby positive charges [specifically of the $\alpha\beta\alpha\beta$ isomer] borne by the trimethylanilinium substituents." Computational results from our group support this argument for the $\alpha\beta\alpha\beta$ isomer.[15] However, the results from this work suggest that the specific orientation of the $[N(CH_3)_3]^+$ cations may be less significant than the overall charge and electron-withdrawing nature of the *o*-$[N(CH_3)_3]^+$ groups.[50]

CONCLUSIONS

The addition of well-positioned charged groups to molecular, inorganic complexes is an increasingly popular topic and has garnered significant attention in the molecular electrocatalysis literature. Here we report the synthesis and characterization of all four atropisomers of iron(III) tetra(*o*-*N*,*N*,*N*-trimethylanilinium)porphyrin pentatriflate and the corresponding reduced iron(II) tetratriflate salts. Each of these complexes contains four spatially resolved, cationic functional groups that are uniquely arranged around a redox-active iron. The single-crystal X-ray structures and ^{1}H NMR spectra show the nature and high purity of the separate atropisomers that are available from this revised synthesis. The previously reported synthesis is

https://doi.org/10.1021/acs.inorgchem.1c00236
Inorg. Chem. 2021, 60, 5240−5251

shown to form a mixture of atropisomers because rotamerization occurred upon heating in one of the steps after the atropisomer separation. Material from the prior synthesis, incorrectly assumed to be the single $\alpha\beta\alpha\beta$ isomer, was used in an earlier study of CO_2 reduction electrocatalysis[10] and in our earlier paper on O_2 reduction.[12] Because the CO_2 reduction study is currently the leading molecular CO_2-to-CO catalyst in combined turnover frequency and overpotential and has been highly cited, the actual multiple-isomer nature of the catalyst present in those solutions is of significance.

The impact of unique charge positioning around the iron center was probed by examining the properties of these atropisomers. The single-crystal X-ray structures suggest that triflate binding to the iron center is enhanced by electrostatics much more strongly in the $\alpha\alpha\alpha\alpha$ isomer, where the charges all lie on the same side of the molecule. The ferric and ferrous $\alpha\alpha\alpha\alpha$ structures also have layered packing arrangements in the solid state, different from the more typical 3D packing seen in the other structures. In contrast, the electrochemistry of the atropisomers was almost unaffected by the orientation of the charged groups, with their Fe^{III}/Fe^{II} reduction potentials all being within ~20 mV, in both MeCN and DMF. Yet the *ortho*-positioning of the cationic groups is clearly important, as these potentials are hundreds of millivolts more positive than the $E_{1/2}$ values for the structural isomer containing the same cationic groups in the *para* position. These trends are rationalized, at least in part, by a simple electrostatic conductive-sphere model. Overall, the studies described here show the varied effects of positioned charges in a metal complex, and they provide guidelines for future catalyst designs.

EXPERIMENTAL METHODS

See the Supporting Information for more complete descriptions and for experiments not discussed here.

Synthesis. An atropisomeric mixture of 5,10,15,20-tetra(*o*-aminophenyl)porphyrin was prepared from the sequential (i) condensation of pyrrole and 2-nitrobenzaldehyde and (ii) reduction of the resulting 5,10,15,20-tetra(*o*-nitrophenyl)porphyrin, following literature methods.[28] Each of the four atropisomers was isolated by repeated chromatography on silica with ^{1}H NMR spectra that matched reported spectra (Figures S5−S8).[28]

5,10,15,20-Tetra(o-aminophenyl)porphyrin. ($\alpha\beta\alpha\beta$). ^{1}H NMR (CD_3Cl, ppm): 8.91 (s, 8H), 7.87 (d, 4H), 7.60 (t, 4H), 7.16 (t, 4H), 7.11 (d, 4H), 3.50 (s, 8H), and −2.67 (s, 2H). HRMS (ESI/Q-TOF): m/z $[M + H]^+$ calcd for $[C_{44}H_{35}N_8]^+$, 675.298; found 675.30.

($\alpha\alpha\beta\beta$). ^{1}H NMR (CD_3Cl, ppm): 8.90 (s, 8H), 7.84 (d, 4H), 7.60 (t, 4H), 7.16 (t, 4H), 7.11 (d, 4H), 3.55 (s, 8H), and −2.68 (s, 2H). HRMS (ESI/Q-TOF): m/z $[M + H]^+$ calcd for $[C_{44}H_{35}N_8]^+$, 675.298; found 675.30.

($\alpha\alpha\alpha\beta$). ^{1}H NMR (CD_3Cl, ppm): 8.90 (s, 8H), 7.85 (m, 4H), 7.60 (t, 4H), 7.17 (m, 4H), 7.11 (m, 4H), 3.54 (br s, 8H), and −2.68 (s, 2H). HRMS (ESI/Q-TOF): m/z $[M + H]^+$ calcd for $[C_{44}H_{35}N_8]^+$, 675.298; found 675.30.

($\alpha\alpha\alpha\alpha$). ^{1}H NMR (CD_3Cl, ppm): 8.92 (s, 8H), 7.89 (d, 4H), 7.62 (t, 4H), 7.21 (m, 4H), 7.13 (d, 4H), 3.54 (s, 8H), and −2.66 (s, 2H). HRMS (ESI/Q-TOF): m/z $[M + H]^+$ calcd for $[C_{44}H_{35}N_8]^+$, 675.298; found 675.30.

The atropisomers were methylated by reductive amination using formaldehyde and sodium cyanoborohydride (4 h at 15 °C) and purified by chromatography on silica (Figures S10−S13). The ^{1}H NMR spectrum for the $\alpha\beta\alpha\beta$ isomer matched the literature.[10]

5,10,15,20-Tetra(o-N,N-dimethylaminophenyl)porphyrin. ($\alpha\beta\alpha\beta$). ^{1}H NMR (CD_3Cl, ppm): 8.75 (s, 8H), 8.00 (d, 4H), 7.69 (t, 4H), 7.41 (d, 4H), 7.30 (t, 4H), 2.23 (s, 24H), and −2.30 (s, 2H). HRMS (ESI/Q-TOF): m/z $[M + H]^+$ calcd for $[C_{52}H_{51}N_8]^+$, 787.424; found 787.43.

($\alpha\alpha\beta\beta$). ^{1}H NMR (CD_3Cl, ppm): 8.76 (s, 4H), 8.76 (s, 4H), 7.90 (d, 4H), 7.68 (t, 4H), 7.40 (d, 4H), 7.29 (t, 4H), 2.25 (s, 24H), and −2.32 (s, 2H). HRMS (ESI/Q-TOF): m/z $[M + H]^+$ calcd for $[C_{52}H_{51}N_8]^+$, 787.424; found 787.43.

($\alpha\alpha\alpha\beta$). ^{1}H NMR (CD_3Cl, ppm): 8.76 (s, 4H), 8.75 (s, 4H), 7.90 (m, 4H), 7.68 (m, 4H), 7.41 (m, 4H), 7.28 (m, 4H), 2.30 (s, 12H), 2.27 (s, 6H), 2.23 (s, 6H), and −2.30 (s, 2H). HRMS (ESI/Q-TOF): m/z $[M + H]^+$ calcd for $[C_{52}H_{51}N_8]^+$, 787.424; found 787.42.

($\alpha\alpha\alpha\alpha$). ^{1}H NMR (CD_3Cl, ppm): 8.75 (s, 8H), 7.86 (d, 4H), 7.70 (t, 4H), 7.46 (d, 4H), 7.28 (t, 4H), 2.37 (s, 24H), and −2.25 (s, 2H). HRMS (ESI/Q-TOF): m/z $[M + H]^+$ calcd for $[C_{52}H_{51}N_8]^+$, 787.424; found 787.43.

The iron(III) chloride tetra(*o-N,N*-dimethylaminophenyl)-porphyrins were prepared by transmetalation of the corresponding dilithium porphyrin salts—generated *in situ*—with $FeBr_2(THF)_2$.[32] The ^{1}H NMR spectra are far more complicated for these iron(III) chloride metalloporphyrins due to slow chloride exchange but are qualitatively unique and are reported in Figures S15−S18.

The iron(III) tetra(*o-N,N,N*-trimethylanilinium)porphyrin pentatriflate salts were prepared by using methyl triflate in trimethyl phosphate following a modified literature procedure (Figures S20−S23; see the Supporting Information and discussion above).[15,18] After recrystallization by vapor diffusion of Et_2O into MeCN solutions containing the porphyrins, lustrous purple crystals were collected for all four products. The crystals of the $\alpha\beta\alpha\beta$, $\alpha\alpha\beta\beta$, and $\alpha\alpha\alpha\alpha$ atropisomers were suitable for single-crystal X-ray diffraction.

Iron(III) Tetra(o-N,N,N-trimethylanilinium)porphyrin Pentatriflate. ($\alpha\beta\alpha\beta$). ^{1}H NMR (CD_3CN, ppm): 15.0 (4H, Ar−*H*), 14.6 (8H, pyrr−*H*), 10.53 (4H, Ar−*H*), 10.22 (4H, Ar−*H*), 9.90 (4H, Ar−*H*), and 2.22 (36H, $-(CH_3)_{12}$). HRMS (ESI/Q-TOF): m/z $[M - 4(OTf)]^{4+}$ calcd for $[C_{57}H_{60}N_8FeO_3SF_3]^{4+}$, 262.345; found 262.34.

($\alpha\alpha\beta\beta$). ^{1}H NMR (CD_3CN, ppm): 46.0 (4H, pyrr−*H*), 45.6 (4H, pyrr−*H*), 13.49 (4H, Ar−*H*), 10.70 (4H, Ar−*H*), 10.47 (4H, Ar−*H*), 9.66 (4H, Ar−*H*), and 4.03 (36H, $-(CH_3)_{12}$). HRMS (ESI/Q-TOF): m/z $[M - 4(OTf)]^{4+}$ calcd for $[C_{57}H_{60}N_8FeO_3SF_3]^{4+}$, 262.345; found 262.34.

($\alpha\alpha\alpha\beta$). ^{1}H NMR (CD_3CN, ppm): 34.0 (8H, pyrr−*H*), 14.57−9.32 (16H, Ar−*H*), 5.33 (9H, $-(CH_3)_3$), 3.26 (18H, $-(CH_3)_6$), and 2.60 (9H, $-(CH_3)_3$). HRMS (ESI/Q-TOF): m/z $[M - 4(OTf)]^{4+}$ calcd for $[C_{57}H_{60}N_8FeO_3SF_3]^{4+}$, 262.345; found 262.34.

($\alpha\alpha\alpha\alpha$). ^{1}H NMR (CD_3CN, ppm): 47.6 (8H, pyrr−*H*), 13.36 (4H, Ar−*H*), 10.80 (4H, Ar−*H*), 10.48 (4H, Ar−*H*), 9.62 (4H, Ar-*H*), and 4.29 (36H, $-(CH_3)_{12}$). HRMS (ESI/Q-TOF): m/z $[M - 4(OTf)]^{4+}$ calcd for $[C_{57}H_{60}N_8FeO_3SF_3]^{4+}$, 262.345; found 262.34.

The reduced iron(II) tetra(*o-N,N,N*-trimethylanilinium)porphyrin tetratriflate complexes were prepared by stirring the ferric porphyrin salts with solid Zn(Hg) amalgam in the glovebox, following a reported procedure. The porphyrin products were then precipitated by vapor diffusion of Et_2O into the collected MeCN solutions (Figures S29−S32). As before, purple crystals were collected, all of which were suitable for single-crystal X-ray diffraction. The ^{1}H NMR spectrum for the $\alpha\beta\alpha\beta$ atropisomer matched the reported spectrum.[15]

Iron(II) Tetra(o-N,N,N-trimethylanilinium)porphyrin Tetratriflate. ($\alpha\beta\alpha\beta$). ^{1}H NMR (CD_3CN, ppm): 8.56 (s, 8H, pyrr−*H*), 8.54 (d, 4H, Ar−*H*), 8.24 (d, 4H, Ar−*H*), 8.09 (t, 4H, Ar−*H*), 7.99 (t, 4H, Ar−*H*), and 3.05 (s, 36H, $-(CH_3)_{12}$).

($\alpha\alpha\beta\beta$). ^{1}H NMR (CD_3CN, ppm): 8.86 (s, 4H, pyrr−*H*), 8.83 (s, 4H, Ar−*H*), 8.30 (d, 4H, Ar−*H*), 8.28 (d, 4H, Ar−*H*), 8.08 (t, 4H, Ar−*H*), 7.87 (t, 4H, Ar−*H*), 3.15 (s, 36H, $-(CH_3)_{12}$).

($\alpha\alpha\alpha\beta$). ^{1}H NMR (CD_3CN, ppm): 8.87 (m, 8H, pyrr−*H*), 8.51 (d, 1H, Ar−*H*), 8.44 (d, 2H, Ar−*H*), 8.36 (d, 1H, Ar−*H*), 8.26 (d, 4H, Ar−*H*), 8.07 (m, 4H, Ar−*H*), 7.96 (t, 1H, Ar−*H*), 7.93 (t, 2H, Ar−*H*), 7.77 (t, 1H, Ar−*H*), 3.32 (s, 9H, $-(CH_3)_3$), 3.07 (s, 18H, $-(CH_3)_6$), 3.04 (s, 9H, $-(CH_3)_3$).

($\alpha\alpha\alpha\alpha$). ^{1}H NMR (CD_3CN, ppm): 10.80 (br s, 8H, pyrr−*H*), 8.30 (d, 4H, Ar−*H*), 8.22 (d, 4H, Ar−*H*), 8.06 (t, 4H, Ar−*H*), 7.82 (4H, Ar−*H*), 3.22 (s, 36H, $-(CH_3)_{12}$).

Column Conditions for Isolating the Atropisomers of 5,10,15,20-Tetra(*o*-aminophenyl)porphyrin. $\alpha\beta\alpha\beta$: Column 1 was an 8 in. × 3 in. column of silica, slurry loaded with DCM. The

https://doi.org/10.1021/acs.inorgchem.1c00236
Inorg. Chem. 2021, 60, 5240−5251

αβαβ and *ααββ* atropisomers were separated from the *αααβ* and *αααα* isomers by flash chromatography using 80:20 DCM/Et_2O eluent (R_f = 0.8 and 0.7). The ratio of *αβαβ* to *ααββ* in the collected fractions was approximately 1:2, consistent with the statistical mixture of isomers. Column 2 was an 8 in. × 2 in. column of silica, slurry loaded with DCM. Using a 90:10 DCM/Et_2O eluent, the bulk of the *αβαβ* atropisomer was separated from the *ααββ* (R_f = 0.7 and 0.5). The ratio of *αβαβ* to *ααββ* in the collected fractions was atropisomerically enriched, though often still impure (9:1). The dimensions and eluent mixture for column 3 was the same as column 2. Only the first few fractions were collected and carefully monitored by TLC for contamination by the *ααββ* atropisomer. After combining fractions and removing the solvent, we obtained the *αβαβ* atropisomer with high purity.

ααββ: Columns 1, 2, and 3 were the same as described above for the isolation of the *αβαβ* atropisomer. Fractions of *ααββ* were collected and carefully monitored by TLC for trace *αααβ* and *αβαβ* contamination in the second and third columns (R_f = 0.7, 0.5, and 0.2, respectively). It is worth noting that the solubility of this porphyrin in DCM is lowest of the atropisomers, and so care should be taken to avoid overloading the columns. In general, the *ααββ* isomer was the easiest atropisomer to purify.

αααβ: The dimension of column 1 is the same as described above. After eluting the *αβαβ* and *ααββ* atropisomers by using 80:20 DCM/Et_2O, the *αααβ* could be obtained by eluting with 50:50 DCM/Et_2O (R_f = 0.8). Columns 2 and 3 were the same dimensions as described above and used the same two-stage eluant mixtures (80:20 followed by 50:50 DCM/Et_2O). Care should be taken to avoid contamination by the *ααββ* atropisomer.

αααα: The dimension of column 1 is the same as described above. After eluting the column with 50:50 DCM/Et_2O, we eluted the *αααα* aminophenylporphyrin using 50:50 acetone/Et_2O (R_f = 0.9). Columns 2 and 3 were the same dimensions as those used above but were loaded with 50:50 DCM/Et_2O and eluted with the same mixture until the eluent was clear. The *αααα* porphyrin was obtained in high atropisomeric purity by final elution with 50:50 acetone/Et_2O. Of note, the *αααα* isomer could be conveniently enriched prior to column 1 by refluxing the statistical mixture of atropisomers in the presence of silica.[51]

■ ASSOCIATED CONTENT

Supporting Information

The Supporting Information is available free of charge at https://pubs.acs.org/doi/10.1021/acs.inorgchem.1c00236.

Extended methods, ^1H NMR spectra, mass spectra, UV−vis spectra, and tabulated crystallographic data (PDF)

Accession Codes

CCDC 2056956−2056961 contain the supplementary crystallographic data for this paper. These data can be obtained free of charge via www.ccdc.cam.ac.uk/data_request/cif, or by emailing data_request@ccdc.cam.ac.uk, or by contacting The Cambridge Crystallographic Data Centre, 12 Union Road, Cambridge CB2 1EZ, UK; fax: +44 1223 336033.

■ AUTHOR INFORMATION

Corresponding Author

James M. Mayer − *Department of Chemistry, Yale University, New Haven, Connecticut 06520-8107, United States;* orcid.org/0000-0002-3943-5250; Email: james.mayer@yale.edu

Authors

Daniel J. Martin − *Department of Chemistry, Yale University, New Haven, Connecticut 06520-8107, United States;* orcid.org/0000-0003-2039-592X

Brandon Q. Mercado − *Department of Chemistry, Yale University, New Haven, Connecticut 06520-8107, United States*

Complete contact information is available at: https://pubs.acs.org/10.1021/acs.inorgchem.1c00236

Author Contributions

D.J.M. and J.M.M. conceived the project, constructed the scientific arguments, and wrote the paper. B.Q.M. performed X-ray crystallography and solved the structures. D.J.M. performed all other experiments and analyzed/interpreted the data.

Notes

The authors declare no competing financial interest.

■ ACKNOWLEDGMENTS

This research was supported as part of the Center for Molecular Electrocatalysis, an Energy Frontier Research Center funded by the U.S. Department of Energy (DOE), Office of Science, Office of Basic Energy Sciences. D.J.M. gratefully acknowledges support from a National Science Foundation Graduate Research Fellowship.

■ REFERENCES

(1) Fried, S. D.; Boxer, S. G. Electric Fields and Enzyme Catalysis. *Annu. Rev. Biochem.* **2017**, *86* (1), 387−415.

(2) Warshel, A.; Sharma, P. K.; Kato, M.; Xiang, Y.; Liu, H.; Olsson, M. H. Electrostatic basis for enzyme catalysis. *Chem. Rev.* **2006**, *106* (8), 3210−35.

(3) Shaik, S.; Mandal, D.; Ramanan, R. Oriented electric fields as future smart reagents in chemistry. *Nat. Chem.* **2016**, *8* (12), 1091−1098.

(4) Elgrishi, N.; Rountree, K. J.; McCarthy, B. D.; Rountree, E. S.; Eisenhart, T. T.; Dempsey, J. L. A Practical Beginner's Guide to Cyclic Voltammetry. *J. Chem. Educ.* **2018**, *95* (2), 197−206.

(5) Rountree, E. S.; McCarthy, B. D.; Eisenhart, T. T.; Dempsey, J. L. Evaluation of Homogeneous Electrocatalysts by Cyclic Voltammetry. *Inorg. Chem.* **2014**, *53* (19), 9983−10002.

(6) Costentin, C.; Robert, M.; Savéant, J. M. Current Issues in Molecular Catalysis Illustrated by Iron Porphyrins as Catalysts of the CO_2-to-CO Electrochemical Conversion. *Acc. Chem. Res.* **2015**, *48* (12), 2996−3006.

(7) Costentin, C.; Savéant, J.-M. Multielectron, Multistep Molecular Catalysis of Electrochemical Reactions: Benchmarking of Homogeneous Catalysts. *ChemElectroChem.* **2014**, *1* (7), 1226−1236.

(8) Chantarojsiri, T.; Reath, A. H.; Yang, J. Y. Cationic Charges Leading to an Inverse Free-Energy Relationship for N-N Bond Formation by Mn(VI) Nitrides. *Angew. Chem., Int. Ed.* **2018**, *57* (43), 14037−14042.

(9) Nichols, A. W.; Machan, C. W. Secondary-Sphere Effects in Molecular Electrocatalytic CO_2 Reduction. *Front. Chem.* **2019**, *7*, 397.

(10) Azcarate, I.; Costentin, C.; Robert, M.; Savéant, J. M. Through-Space Charge Interaction Substituent Effects in Molecular Catalysis Leading to the Design of the Most Efficient Catalyst of CO_2-to-CO Electrochemical Conversion. *J. Am. Chem. Soc.* **2016**, *138* (51), 16639−16644.

(11) Zhang, R.; Warren, J. J. Controlling the Oxygen Reduction Selectivity of Asymmetric Cobalt Porphyrins by Using Local Electrostatic Interactions. *J. Am. Chem. Soc.* **2020**, *142* (31), 13426−13434.

(12) Martin, D. J.; Mercado, B. Q.; Mayer, J. M. Combining scaling relationships overcomes rate versus overpotential trade-offs in O_2 molecular electrocatalysis. *Sci. Adv.* **2020**, *6* (11), No. eaaz3318.

(13) Margarit, C. G.; Asimow, N. G.; Gonzalez, M. I.; Nocera, D. G. Double Hangman Iron Porphyrin and the Effect of Electrostatic Nonbonding Interactions on Carbon Dioxide Reduction. *J. Phys. Chem. Lett.* **2020**, *11* (5), 1890−1895.

(14) Sampson, M. D.; Kubiak, C. P. Manganese Electrocatalysts with Bulky Bipyridine Ligands: Utilizing Lewis Acids To Promote Carbon Dioxide Reduction at Low Overpotentials. *J. Am. Chem. Soc.* **2016**, *138* (4), 1386−93.
(15) Martin, D. J.; Johnson, S. I.; Mercado, B. Q.; Raugei, S.; Mayer, J. M. Intramolecular Electrostatic Effects on O_2, CO_2, and Acetate Binding to a Cationic Iron Porphyrin. *Inorg. Chem.* **2020**, *59* (23), 17402−17414.
(16) Kalyanasundaram, K.; Neumannspallart, M. Photophysical and Redox Properties of Water-Soluble Porphyrins in Aqueous-Media. *J. Phys. Chem.* **1982**, *86* (26), 5163−5169.
(17) Kano, K.; Minamizono, H.; Kitae, T.; Negi, S. Self-Aggregation of Cationic Porphyrins in Water. Can π-π Stacking Interaction Overcome Electrostatic Repulsive Force? *J. Phys. Chem. A* **1997**, *101* (34), 6118−6124.
(18) La, T.; Richards, R.; Miskelly, G. M. Synthesis and Characterization of the Cationic Porphyrin Meso-Tetrakis(2,3,5,6-Tetrafluoro-*N*,*N*,*N*-Trimethyl-4-Aniliniumyl)Porphyrin. *Inorg. Chem.* **1994**, *33* (14), 3159−3163.
(19) Miskelly, G. M.; Webley, W. S.; Clark, C. R.; Buckingham, D. A. Acidity and dimerization of three water-soluble iron(III) porphyrin cations: (meso-$\alpha,\beta,\alpha,\beta$-tetrakis(o-(N-methylnicotinamido)phenyl)-porphyrinato)iron(III), (meso-$\alpha,\alpha,\alpha,\alpha$-tetrakis(o-(N-methylnicotinamido)phenyl)porphyrinato)iron(III), and (meso-tetrakis(1-methylpyridinium-4-yl)porphyrinato)iron(III). *Inorg. Chem.* **1988**, *27* (21), 3773−3781.
(20) Tovmasyan, A.; Weitner, T.; Sheng, H.; Lu, M.; Rajic, Z.; Warner, D. S.; Spasojevic, I.; Reboucas, J. S.; Benov, L.; Batinic-Haberle, I. Differential coordination demands in Fe versus Mn water-soluble cationic metalloporphyrins translate into remarkably different aqueous redox chemistry and biology. *Inorg. Chem.* **2013**, *52* (10), 5677−91.
(21) Batinić-Haberle, I.; Spasojević, I.; Hambright, P.; Benov, L.; Crumbliss, A. L.; Fridovich, I. Relationship among Redox Potentials, Proton Dissociation Constants of Pyrrolic Nitrogens, and in Vivo and in Vitro Superoxide Dismutating Activities of Manganese(III) and Iron(III) Water-Soluble Porphyrins. *Inorg. Chem.* **1999**, *38* (18), 4011−4022.
(22) Weitner, T.; Budimir, A.; Kos, I.; Batinic-Haberle, I.; Birus, M. Acid-base and electrochemical properties of manganese meso(ortho- and meta-*N*-ethylpyridyl)porphyrins: potentiometric, spectrophotometric and spectroelectrochemical study of protolytic and redox equilibria. *Dalton Trans.* **2010**, *39* (48), 11568−76.
(23) Franke, A.; Scheitler, A.; Kenkel, I.; Lippert, R.; Zahl, A.; Balbinot, D.; Jux, N.; Ivanovic-Burmazovic, I. Positive Charge on Porphyrin Ligand and Nature of Metal Center Define Basic Physicochemical Properties of Cationic Manganese and Iron Porphyrins in Aqueous Solution. *Inorg. Chem.* **2019**, *58* (15), 9618−9630.
(24) Brausam, A.; Eigler, S.; Jux, N.; van Eldik, R. Mechanistic investigations of the reaction of an iron(III) octa-anionic porphyrin complex with hydrogen peroxide and the catalyzed oxidation of diammonium-2,2′-azinobis(3-ethylbenzothiazoline-6-sulfonate). *Inorg. Chem.* **2009**, *48* (16), 7667−78.
(25) Jee, J. E.; Eigler, S.; Hampel, F.; Jux, N.; Wolak, M.; Zahl, A.; Stochel, G.; van Eldik, R. Kinetic and mechanistic studies on the reaction of nitric oxide with a water-soluble octa-anionic iron(III) porphyrin complex. *Inorg. Chem.* **2005**, *44* (22), 7717−31.
(26) Jee, J. E.; Wolak, M.; Balbinot, D.; Jux, N.; Zahl, A.; van Eldik, R. A comparative mechanistic study of the reversible binding of NO to a water-soluble octa-cationic Fe(III) porphyrin complex. *Inorg. Chem.* **2006**, *45* (3), 1326−37.
(27) Jee, J. E.; Eigler, S.; Jux, N.; Zahl, A.; van Eldik, R. Influence of an extremely negatively charged porphyrin on the reversible binding kinetics of NO to Fe(III) and the subsequent reductive nitrosylation. *Inorg. Chem.* **2007**, *46* (8), 3336−52.
(28) Collman, J. P.; Gagne, R. R.; Reed, C. A.; Halbert, T. R.; Lang, G.; Robinson, W. T. Picket fence porphyrins. Synthetic models for oxygen binding hemoproteins. *J. Am. Chem. Soc.* **1975**, *97* (6), 1427−39.
(29) Nishino, N.; Kobata, K.; Mihara, H.; Fujimoto, T. Efficient Preparation of $\alpha\beta\alpha\beta$-Atropisomer of meso-Tetra(o-aminophenyl)-porphyrin. *Chem. Lett.* **1992**, *21* (10), 1991−1994.
(30) Rose, E.; Cardonpilotaz, A.; Quelquejeu, M.; Bernard, N.; Kossanyi, A.; Desmazieres, B. Efficient Preparation of the $\alpha,\alpha,\beta,\beta$-Atropoisomer of meso-Tetrakis(o-aminophenyl)porphyrin. *J. Org. Chem.* **1995**, *60* (12), 3919−3920.
(31) Rose, E.; Quelquejeu, M.; Pochet, C.; Julien, N.; Kossanyi, A.; Hamon, L. Large-scale preparation of $\alpha,\beta,\alpha,\beta$ atropisomer of meso-Tetrakis(o-aminophenyl)porphyrin. *J. Org. Chem.* **1993**, *58* (19), 5030−5031.
(32) Arnold, J.; Dawson, D. Y.; Hoffman, C. G. Synthesis and Characterization of Lithium, Sodium, and Potassium Porphyrin Complexes - X-Ray Crystal-Structures of $Li_2(C_6H_{12}O_2)_2$TMPP, $Na_2(THF)_4$OEP, and K_2(pyridine)$_4$OEP. *J. Am. Chem. Soc.* **1993**, *115* (7), 2707−2713.
(33) Boersma, A. D.; Goff, H. M. Multinuclear magnetic resonance spectroscopy of spin-admixed S = 5/2, 3/2 iron(III) porphyrins. *Inorg. Chem.* **1982**, *21* (2), 581−586.
(34) Safo, M. K.; Nesset, M. J. M.; Walker, F. A.; Debrunner, P. G.; Scheidt, W. R. Models of the Cytochromes. Axial Ligand Orientation and Complex Stability in Iron(II) Porphyrinates: The Case of the Noninteracting d_π Orbitals. *J. Am. Chem. Soc.* **1997**, *119* (40), 9438−9448.
(35) Walker, F. A.; Simonis, U. *Iron Porphyrin Chemistry*; John Wiley & Sons, Ltd.: Chichester, UK, 2006.
(36) Pegis, M. L.; Martin, D. J.; Wise, C. F.; Brezny, A. C.; Johnson, S. I.; Johnson, L. E.; Kumar, N.; Raugei, S.; Mayer, J. M. Mechanism of Catalytic O_2 Reduction by Iron Tetraphenylporphyrin. *J. Am. Chem. Soc.* **2019**, *141*, 8315−8326.
(37) Tomé, A. C.; Silva, A. M. S.; Alkorta, I.; Elguero, J. Atropisomerism and conformational aspects of meso-tetraarylporphyrins and related compounds. *J. Porphyrins Phthalocyanines* **2011**, *15* (01), 1−28.
(38) Zimmer, B.; Bulach, V.; Drexler, C.; Erhardt, S.; Hosseini, M. W.; De Cian, A. Design, synthesis, structural analysis and atropoisomerisation studies of polynucleating ligands based on porphyrins bearing catechol units. *New J. Chem.* **2002**, *26* (1), 43−57.
(39) Crossley, M. J.; Field, L. D.; Forster, A. J.; Harding, M. M.; Sternhell, S. Steric Effects on Atropisomerism in Tetraarylporphyrins. *J. Am. Chem. Soc.* **1987**, *109* (2), 341−348.
(40) Nozawa, R.; Tanaka, H.; Cha, W. Y.; Hong, Y.; Hisaki, I.; Shimizu, S.; Shin, J. Y.; Kowalczyk, T.; Irle, S.; Kim, D.; Shinokubo, H. Stacked antiaromatic porphyrins. *Nat. Commun.* **2016**, *7*, 13620.
(41) Kadish, K. M.; Morrison, M. M.; Constant, L. A.; Dickens, L.; Davis, D. G. A study of solvent and substituent effects on the redox potentials and electron-transfer rate constants of substituted iron meso-tetraphenylporphyrins. *J. Am. Chem. Soc.* **1976**, *98* (26), 8387−90.
(42) Romelt, C.; Song, J.; Tarrago, M.; Rees, J. A.; van Gastel, M.; Weyhermuller, T.; DeBeer, S.; Bill, E.; Neese, F.; Ye, S. Electronic Structure of a Formal Iron(0) Porphyrin Complex Relevant to CO_2 Reduction. *Inorg. Chem.* **2017**, *56* (8), 4746−4751.
(43) Romelt, C.; Ye, S.; Bill, E.; Weyhermuller, T.; van Gastel, M.; Neese, F. Electronic Structure and Spin Multiplicity of Iron Tetraphenylporphyrins in Their Reduced States as Determined by a Combination of Resonance Raman Spectroscopy and Quantum Chemistry. *Inorg. Chem.* **2018**, *57* (4), 2141−2148.
(44) Pegis, M. L.; McKeown, B. A.; Kumar, N.; Lang, K.; Wasylenko, D. J.; Zhang, X. P.; Raugei, S.; Mayer, J. M. Homogenous Electrocatalytic Oxygen Reduction Rates Correlate with Reaction Overpotential in Acidic Organic Solutions. *ACS Cent. Sci.* **2016**, *2* (11), 850−856.
(45) Nichols, E. M.; Derrick, J. S.; Nistanaki, S. K.; Smith, P. T.; Chang, C. J. Positional effects of second-sphere amide pendants on electrochemical CO_2 reduction catalyzed by iron porphyrins. *Chem. Sci.* **2018**, *9* (11), 2952−2960.
(46) Bonin, J.; Maurin, A.; Robert, M. Molecular catalysis of the electrochemical and photochemical reduction of CO_2 with Fe and Co

https://doi.org/10.1021/acs.inorgchem.1c00236
Inorg. Chem. 2021, 60, 5240−5251

metal based complexes. Recent advances. *Coord. Chem. Rev.* **2017**, *334*, 184−198.
(47) Conway, B. E. *The Electrolyte Factor in Supercapacitor Design and Performance: Conductivity, Ion Pairing and Solvation BT - Electrochemical Supercapacitors: Scientific Fundamentals and Technological Applications*; Conway, B. E., Ed. Springer US: Boston, MA, 1999; pp 335−375.
(48) Wang, P.; Anderko, A. Computation of dielectric constants of solvent mixtures and electrolyte solutions. *Fluid Phase Equilib.* **2001**, *186* (1−2), 103−122.
(49) Parr, R. G.; Pearson, R. G. Absolute Hardness - Companion Parameter to Absolute Electronegativity. *J. Am. Chem. Soc.* **1983**, *105* (26), 7512−7516.
(50) Mao, Y.; Loipersberger, M.; Kron, K. J.; Derrick, J. S.; Chang, C. J.; Sharada, S. M.; Head-Gordon, M. Consistent inclusion of continuum solvation in energy decomposition analysis: theory and application to molecular CO_2 reduction catalysts. *Chem. Sci.* **2021**, *12*, 1398.
(51) Lindsey, J. Increased Yield of a Desired Isomer by Equilibria Displacement on Binding to Silica-Gel, Applied to Meso-Tetrakis(*o*-aminophenyl)Porphyrin. *J. Org. Chem.* **1980**, *45* (25), 5215−5215.

https://doi.org/10.1021/acs.inorgchem.1c00236
Inorg. Chem. 2021, 60, 5240−5251